# Elimination of DC-Link Current Ripple for Modular Multilevel Converters With Capacitor Voltage-Balancing Pulse-Shifted Carrier PWM

Fujin Deng, *Member, IEEE*, and Zhe Chen, *Senior Member, IEEE*

***Abstract*—The modular multilevel converter (MMC) is attractive for medium- and high-power applications because of its high modularity, availability, and power quality. In this paper, the current ripple on the dc link of the three-phase MMC derived from the phase-shifted carrier-based pulse-width modulation scheme is analyzed. A control strategy is proposed for the current ripple elimination. Through the regulation of the phase-shifted angles of the carrier waves in the three phases of the MMC, the current ripple on the dc link of the three-phase MMC can be effectively eliminated. Simulations and experimental studies of the MMC were conducted, and the results confirm the effectiveness of the proposed current ripple elimination control.**

***Index Terms*—Capacitor voltage balancing, control strategy, modular multilevel converter (MMC), ripple elimination.**

## I. Introduction

MODULAR multilevel converters (MMCs) received increasing attentions in recent years due to the demands of high power and high voltage in industrial applications [1]. The MMC was first proposed by Marquardt and Lesnicar in 2000s and is regarded as one of the next-generation high-voltage multilevel converters without line-frequency transformers [2]. The MMC is composed of a number of half-bridge submodules (SMs) converters, which offers redundancy possibilities for higher reliability. The high number of modules can also produce high-level output voltage and enables a significant reduction in the device's average switching frequency without compromising the power quality [3]. In addition, the series-connected buffer inductor in each arm can limit the current and protect the system during faults. Due to its modular structure, simple voltage scaling, the MMC is attractive for medium-voltage drives, high-voltage direct current (HVDC) transmission, and flexible ac transmission systems [4]–[8].

Recently, the MMC has been reported in a few literature works [1]–[25], which focus on pulse width modulation (PWM) method, capacitor voltage balancing control, modeling method, reduction of switching frequency, circulating current-suppressing control, inner energy control, fault detection method, loss analysis, system control under unbalanced grid, and so on. Various multicarrier PWM techniques have been introduced to the MMC, where the phase-disposition (PD) sinusoidal pulse width modulation (SPWM) method and the phase-shifted carrier-based (PSC) PWM method are widely used for the control of the MMC [10]–[18]. The capacitor voltage-balancing is an important issue in the MMC. Hagiwara and Akagi [9] proposed a capacitor voltage-balancing control for the MMC based on the combination of averaging and balancing control without any external circuit, and the results are verified by simulation and experiment. Saeedifard and Iravani [10] presented a capacitor voltage-balancing control method with PD-SPWM method, where the capacitor voltage can be balanced by sorting and selecting the different SMs to be turned ON in each switching period. Deng and Chen [11] presented the PSC-PWM method for capacitor voltage balancing, where a high-frequency arm current may be generated under the PSC-PWM method, and the capacitor voltage-balancing can be realized with the generated high-frequency arm current. However, the generated high-frequency arm current under the PSC-PWM method will be injected into the dc link of the MMC and may produce dc-link current ripple, which has been not discussed.

In this paper, the PSC-PWM method for the three-phase MMC is discussed. The produced high-frequency arm current under the PSC-PWM method in the three phases of the MMC is analyzed. A dc-link current ripple elimination control strategy is proposed for the three-phase MMC, where the high-frequency current ripple on the dc link of the MMC can be eliminated by controlling the phase-shift angles of the carrier waves in the three phases.

This paper is organized as follows. In Section II, the basic structure, modulation, and voltage balancing control of the MMC is presented. Section III proposes the current ripple elimination control for three-phase MMCs. The system simulations and experimental tests are described in Sections IV and V, respectively, to show the effectiveness of the proposed current ripple elimination control. Finally, the conclusions are presented in Section VI.

## II. Modular Multilevel Converters

### A. Structure of MMCs

A schematic representation of the three-phase MMC is shown in Fig. 1(a). The MMC consists of six arms where each arm includes $n$ series-connected SMs and a buffer inductor $L_S$. The upper and lower arms in the same phase comprise a phase

Manuscript received September 7, 2013; revised April 21, 2014, March 26, 2014, and January 5, 2014; accepted April 29, 2014. Date of publication May 9, 2014; date of current version August 26, 2014. This work was supported by the Department of Energy Technology, Aalborg University, Denmark. Recommended for publication by Associate Editor M. A. Perez.

The authors are with the Department of Energy Technology, Aalborg University, Aalborg 9220, Denmark (e-mail: fde@et.aau.dk; zch@et.aau.dk).

Color version of one or more of the figures in this paper are available online at http://ieeexplore.ieee.org.

Digital Object Identifier 10.1109/TPEL.2014.2322913

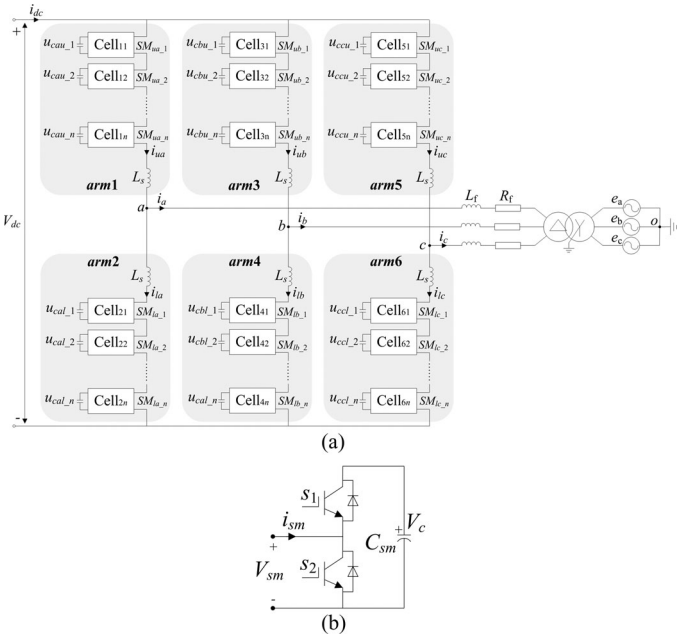


Fig. 1. (a) Block diagram of the three-phase MMC. (b) SM unit.

TABLE I
SM STATE

| SM state | Switch S1 | Switch S2 | $V_{\rm sm}$ | Arm current $i_{\rm sm}$ | Capacitor $C_{\rm sm}$ state | Capacitor voltage $V_c$ |
|---|---|---|---|---|---|---|
| On | ON | OFF | $V_c$ | Positive | Charge | Increased |
| | | | | Negative | Discharge | Decreased |
| Off | OFF | ON | 0 | Positive | Bypass | Unchanged |
| | | | | Negative | Bypass | Unchanged |

unit. An SM unit is shown in Fig. 1(b), which is a half-bridge converter based on two insulated gate bipolar transistors and a dc storage capacitor [13]–[17].

The normal working states of the SM are shown in Table I. The switches (S1 and S2) in the SM unit are controlled with two complementary signals. If S1 is switched ON and S2 is switched OFF, the SM state is "On" and the corresponding output voltage $V_{\rm sm}$ of the SM is $V_c$. On the contrary, the SM state is "Off" and the $V_{\rm sm}$ is 0 when S1 is switched OFF and S2 is switched ON [10].

The capacitor $C_{\rm sm}$ situation in each SM is related to the SM state and the direction of the arm current $i_{\rm sm}$. If the SM state is "On" and the arm current $i_{\rm sm}$ is positive, as shown in Fig. 1(b), $C_{\rm sm}$ would be charged and its voltage $V_c$ increased. Conversely, $C_{\rm sm}$ would be discharged and $V_c$ decreased when the SM state is "On" and $i_{\rm sm}$ is negative. On the other hand, $C_{\rm sm}$ would be bypassed when the SM state is "Off," and its voltage $V_c$ remains unchanged [11].

### B. Modulation and Voltage-Balancing Control

The PSC-PWM modulation [11], which can produce high voltage level, is applied to the MMC, as shown in Fig. 2 with four SMs for each arm. In the phase A of the MMC with *n* SMs

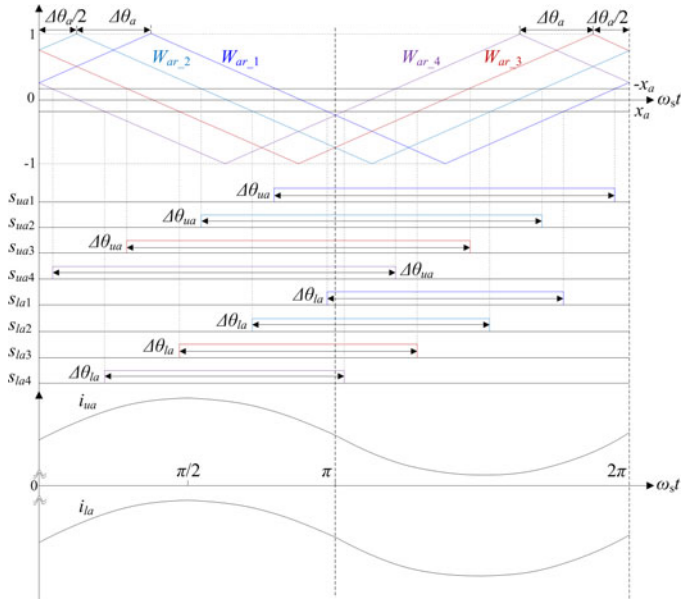


Fig. 2. Block diagram of the PSC-PWM method for phase A.

per arm, the *n* pulses $S_{\rm ua1} \sim S_{\rm uan}$ and $S_{\rm la1} \sim S_{\rm lan}$ for the upper and lower arms can be produced by the comparison of the *n* carrier waves $W_{ar1} \sim W_{arn}$ and the reference signal $-x_a$ and $x_a$, respectively. The carrier wave frequency is $f_s$.$\omega_s = 2\pi f_s$ is the angular frequency of the carrier wave. Each carrier wave is phase-shifted by an angle of $\Delta\theta_a$ ($0 < \Delta\theta_a < 2\pi/n$). Suppose the carrier wave frequency $f_s$ is far higher than that of the reference signal, the generated *n* upper arm pulses $S_{ua_1} \sim S_{uan}$ almost have the same width of $\Delta\theta_{ua}$ and the generated *n* lower arm pulses $S_{la_1} \sim S_{lan}$ almost have the same width of $\Delta\theta_{la}$, as shown in Fig. 2.

Suppose the capacitor voltages are kept the same and according to [11], a high-frequency component $i_{fs\_a}$ in the arm currents $i_{ua}$ and $i_{la}$ of phase A with a frequency of $f_s$ may be generated by the PSC-PWM method, as shown in Fig. 2, which can be expressed as

$$i_{fs\_a}(t) = \frac{2V_c}{\omega_s L_s \pi} \cdot \frac{\sin\frac{n\Delta\theta_a}{2}}{\sin\frac{\Delta\theta_a}{2}} \cdot \cos\left(\frac{\Delta\theta_{ua} - \Delta\theta_{la}}{4}\right) \cdot \sin(\omega_s t). \quad (1)$$

The peak value of the generated high-frequency current appears at $\pi/2$ in each period of $2\pi$, as shown in Fig. 2. The capacitor voltage-balancing control can be realized as Table II [11].

1) When the capacitor voltage is low, the pulse with its middle-point close to $\pi/2$, as shown in Fig. 2, may be assigned to the corresponding SM. Consequently, the corresponding SM capacitor will absorb more power when the arm current is positive and the capacitor voltage increases more. Or, the corresponding SM capacitor will produce less power when the arm current is negative and the capacitor voltage decreases less.
2) When the capacitor voltage is high, the pulse with its middle-point far from $\pi/2$, as shown in Fig. 2, may be assigned to the SM. Consequently, the corresponding SM

TABLE II
SM CAPACITOR VOLTAGE CONTROL

| SM capacitor voltage | Pulse assignment | Arm current | Capacitor energy transfer | SM capacitor voltage trend |
|---|---|---|---|---|
| Low | Pulse with its middle point close to $\pi/2$ | Positive | Absorb more power | Increased more |
| | | Negative | Produce less power | Decreased less |
| High | Pulse with its middle point far away from $\pi/2$ | Positive | Absorb less power | Increased less |
| | | Negative | Produce more power | Decreased more |

capacitor will absorb less power when the arm current is positive and the capacitor voltage increases less. Or, the corresponding SM capacitor will produce more power when the arm current is negative and the capacitor voltage decreases more.

As to the phases B and C, the high-frequency component $i_{fs\_b}$ and $i_{fs\_c}$ in the arm currents of phases B and C with a frequency of $f_s$ may also be generated under the PSC-PWM method, which can also be used for their capacitor voltage-balancing control with the similar method to that for phase A.

## III. PROPOSED CURRENT RIPPLE ELIMINATION CONTROL

In the three-phase MMC, as shown in Fig. 1, the generated high-frequency currents $i_{fs\_a}$, $i_{fs\_b}$, and $i_{fs\_c}$ with the frequency of $f_s$ in phases A, B, and C will be injected into the dc link of the MMC and may cause dc-link current ripple. In order to eliminate the high-frequency current ripple with the frequency of $f_s$ on the dc link of the three-phase MMC, the middle-points $M_1$, $M_2$, and $M_3$ of the triangular carrier waves $W_{ar_1} \sim W_{arn}$, $W_{br_1} \sim W_{brn}$, and $W_{cr_1} \sim W_{crn}$ for phases A, B, and C are proposed to be phase-shifted by an angle of $2\pi/3$, as shown in Fig. 3. Each carrier wave for phases B and C is phase-shifted by an angle of $\Delta\theta_b$ and $\Delta\theta_c$ ($0 < \Delta\theta_b < 2\pi/n, 0 < \Delta\theta_c < 2\pi/n$), respectively, as shown in Fig. 3. Consequently, according to Figs. 2 and 3, the generated high-frequency currents $i_{fs\_b}$ and $i_{fs\_c}$ in phases B and C will lead and lag $i_{fs\_a}$ by an angle of $2\pi/3$.

According to [11] and Figs. 2 and 3, the generated high-frequency currents $i_{fs\_b}$ and $i_{fs\_c}$ under the PSC-PWM method in phases B and C can be expressed as

$$\begin{cases} i_{fs\_b}(t) = \dfrac{2V_c}{\omega_s L_s \pi} \cdot \dfrac{\sin\frac{n\Delta\theta_b}{2}}{\sin\frac{\Delta\theta_b}{2}} \cdot \cos\left(\dfrac{\Delta\theta_{ub} - \Delta\theta_{lb}}{4}\right) \cdot \sin\left(\omega_s t + \dfrac{2\pi}{3}\right) \\ i_{fs\_c}(t) = \dfrac{2V_c}{\omega_s L_s \pi} \cdot \dfrac{\sin\frac{n\Delta\theta_c}{2}}{\sin\frac{\Delta\theta_c}{2}} \cdot \cos\left(\dfrac{\Delta\theta_{uc} - \Delta\theta_{lc}}{4}\right) \cdot \sin\left(\omega_s t - \dfrac{2\pi}{3}\right) \end{cases} \quad (2)$$

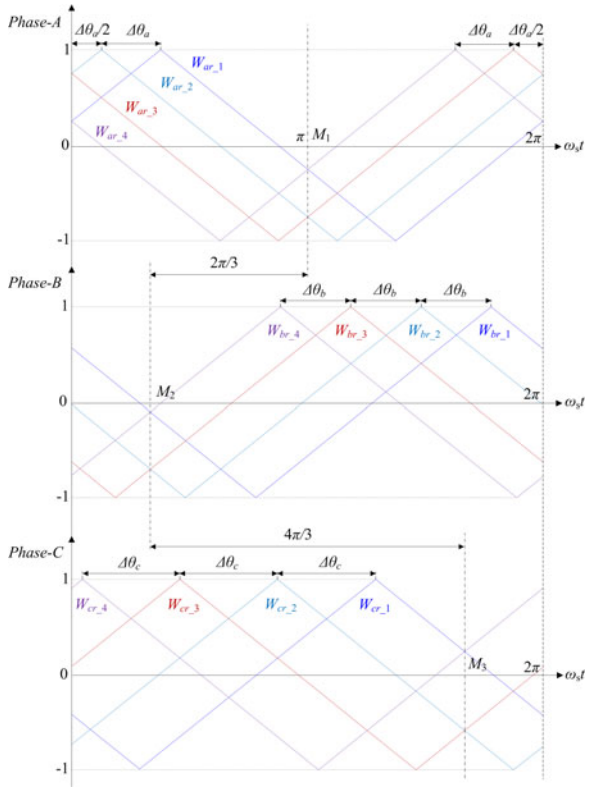


Fig. 3. Block diagram of the PSC waves for phases A, B, and C.

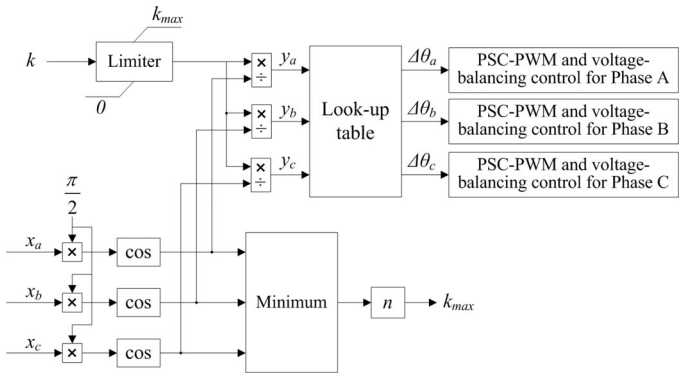


Fig. 4. Block diagram of the proposed current ripple elimination control for three-phase MMCs.

where $\Delta\theta_{ub}$, $\Delta\theta_{lb}$ and $\Delta\theta_{uc}$, $\Delta\theta_{lc}$ are the upper and lower arm pulse widths of phases B and C, respectively. The three-phase sinusoidal reference signals $x_a$, $x_b$, and $x_c$ for the MMC can be defined as

$$\begin{cases} x_a = m \cdot \sin(\omega t + \alpha) \\ x_b = m \cdot \sin(\omega t + \alpha - 2\pi/3) \\ x_c = m \cdot \sin(\omega t + \alpha + 2\pi/3) \end{cases} \quad (3)$$

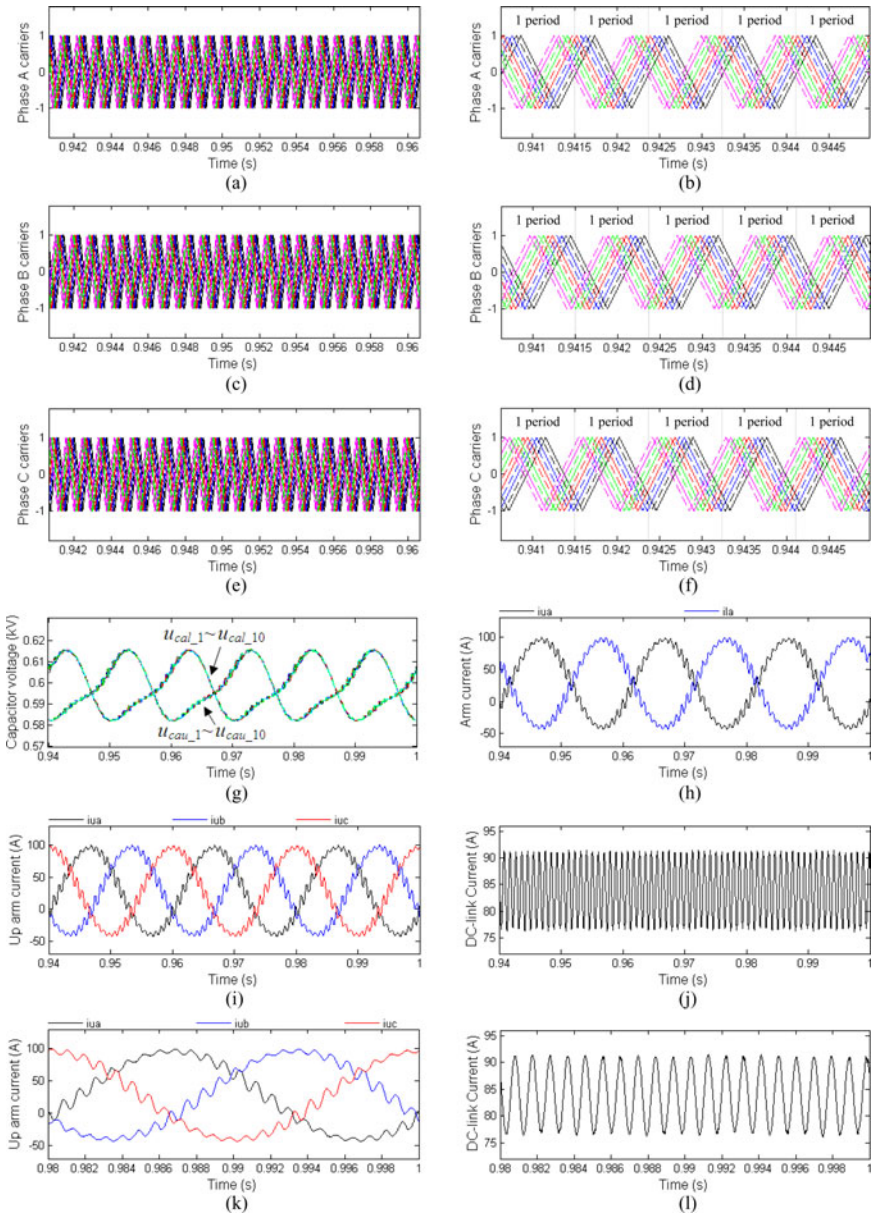


Fig. 5. Simulated waveforms of the MMC without proposed control under $\Delta\theta_a = \Delta\theta_b = \Delta\theta_c = 22°$. (a) Carrier waves for phase A. (b) Carrier waves for phase A in a small time scale. (c) Carrier waves for phase B. (d) Carrier waves for phase B in a small time scale. (e) Carrier waves for phase C. (f) Carrier waves for phase C in a small time scale. (g) Capacitor voltage of phase A. (h) Upper and lower arm currents $i_{ua}$ and $i_{la}$ of phase A. (i) Upper arm currents $i_{ua}$, $i_{ub}$, and $i_{uc}$. (j) DC-link current $i_{\rm dc}$. (k) Upper arm currents $i_{ua}$, $i_{ub}$, and $i_{uc}$ in small time scale. (l) DC-link current $i_{\rm dc}$ in small time scale.

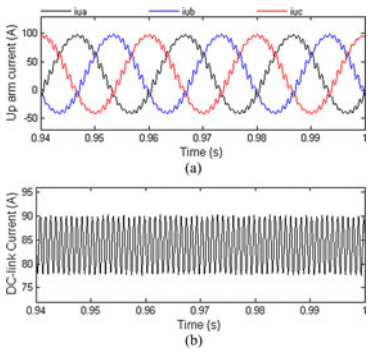


Fig. 6. Simulated waveforms of the MMC without proposed control under $\Delta\theta_a = \Delta\theta_b = \Delta\theta_c = 26°$. (a) Upper arm currents $i_{ua}$, $i_{ub}$, and $i_{uc}$. (b) DC-link current $i_{\rm dc}$.

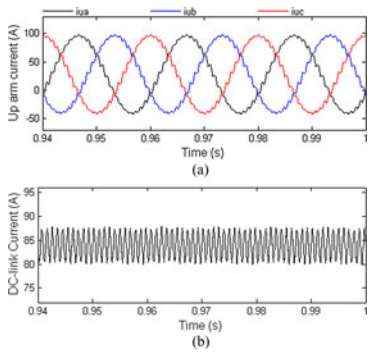


Fig. 7. Simulated waveforms of the MMC without proposed control under $\Delta\theta_a = \Delta\theta_b = \Delta\theta_c = 30°$. (a) Upper arm currents $i_{ua}$, $i_{ub}$, and $i_{uc}$. (b) DC-link current $i_{\rm dc}$.

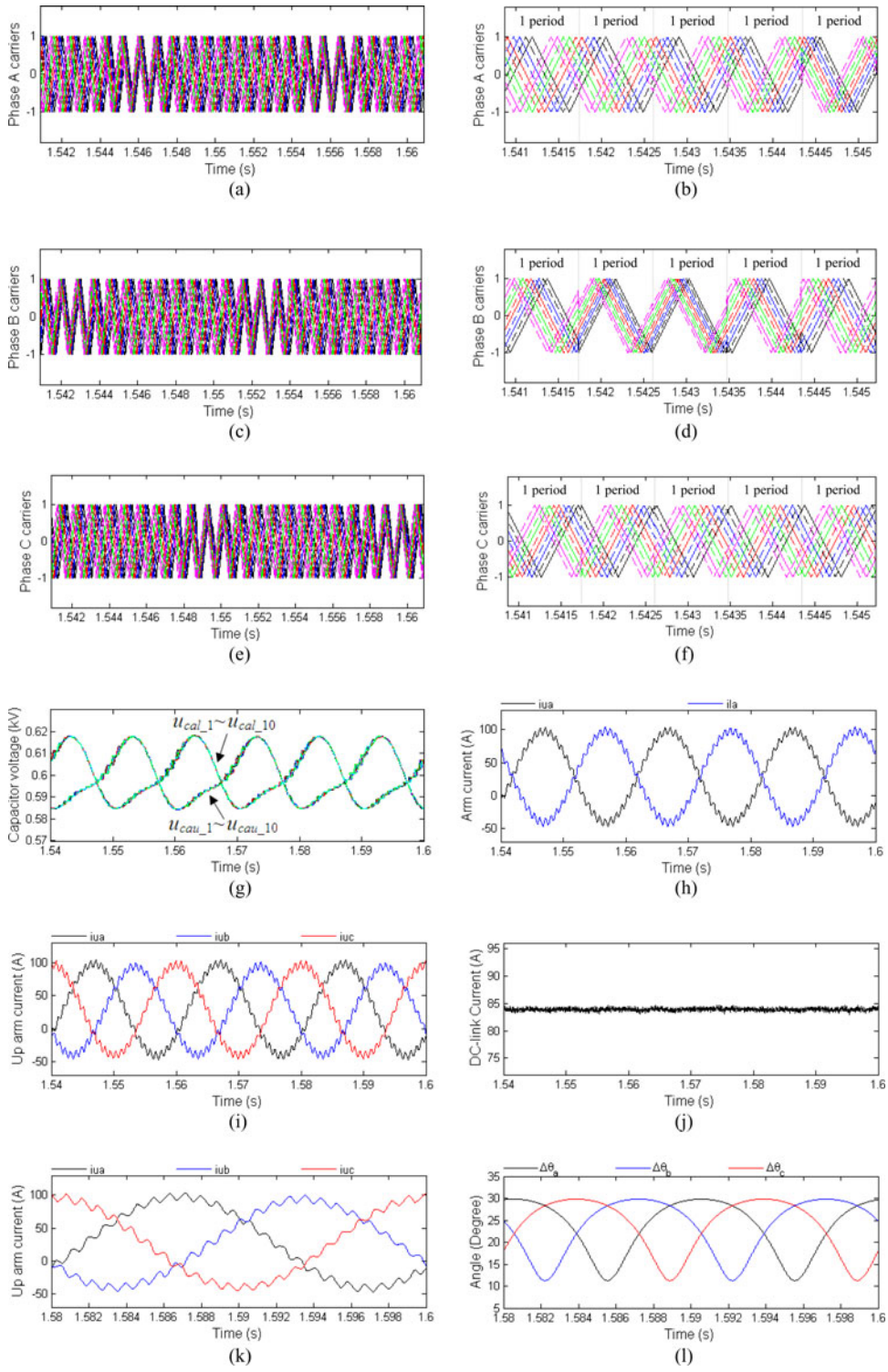


Fig. 8. Simulated waveforms of the MMC with proposed control under $k = 2$. (a) Carrier waves for phase A. (b) Carrier waves for phase A in a small time scale. (c) Carrier waves for phase B. (d) Carrier waves for phase B in a small time scale. (e) Carrier waves for phase C. (f) Carrier waves for phase C in a small time scale. (g) Capacitor voltage of phase A. (h) Upper and lower arm currents $i_{ua}$ and $i_{la}$ of phase A. (i) Upper arm currents $i_{ua}$, $i_{ub}$, and $i_{uc}$. (j) DC-link current $i_{\mathrm{dc}}$. (k) Upper arm currents $i_{ua}$, $i_{ub}$, and $i_{uc}$ in small time scale. (l) Phase-shift angles $\Delta\theta_a$, $\Delta\theta_b$, and $\Delta\theta_c$.

where $m$ is modulation index. $\alpha$ is the phase angle. As to the SPWM method with symmetrical regular sampling [26], the produced pulse widths for the upper and lower arms of phases A, B, and C in each period of $2\pi$, as shown in Fig. 2, can be calculated as

$$\begin{cases} \Delta\theta_{uj} = 2\pi \cdot \dfrac{1+x_j}{2} \\ \Delta\theta_{lj} = 2\pi \cdot \dfrac{1-x_j}{2} \end{cases}, \quad (j = a, b, c). \tag{4}$$

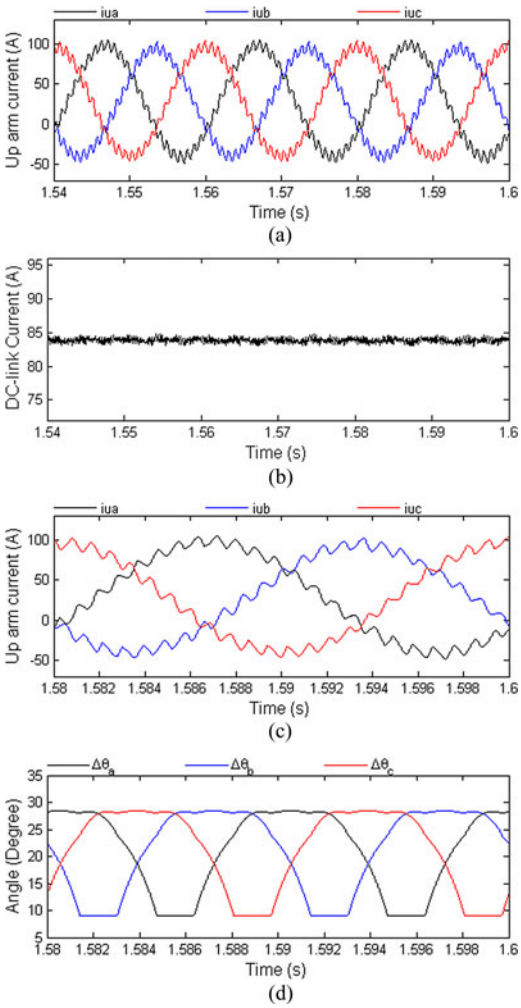


Fig. 9. Simulated waveforms of the MMC with proposed control under $k = 2.5$. (a) Upper arm currents $i_{ua}$, $i_{ub}$, and $i_{uc}$. (b) DC-link current $i_{\rm dc}$. (c) Upper arm currents $i_{ua}$, $i_{ub}$, and $i_{uc}$ in small time scale. (d) Phase-shift angles $\Delta\theta_a$, $\Delta\theta_b$, and $\Delta\theta_c$.

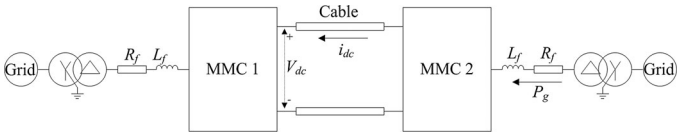


Fig. 10. Block diagram of an MMC-based HVDC system.

Substituting (4) into (1) and (2), there will be

$$\begin{cases} i_{fs\_a}(t) = \dfrac{2V_c}{\omega_s L_s \pi} \cdot \cos\left(\dfrac{\pi}{2}x_a\right) \cdot \dfrac{\sin\frac{n\Delta\theta_a}{2}}{\sin\frac{\Delta\theta_a}{2}} \cdot \sin(\omega_s t) \\ i_{fs\_b}(t) = \dfrac{2V_c}{\omega_s L_s \pi} \cdot \cos\left(\dfrac{\pi}{2}x_b\right) \cdot \dfrac{\sin\frac{n\Delta\theta_b}{2}}{\sin\frac{\Delta\theta_b}{2}} \cdot \sin\left(\omega_s t + \dfrac{2\pi}{3}\right) \\ i_{fs\_c}(t) = \dfrac{2V_c}{\omega_s L_s \pi} \cdot \cos\left(\dfrac{\pi}{2}x_c\right) \cdot \dfrac{\sin\frac{n\Delta\theta_c}{2}}{\sin\frac{\Delta\theta_c}{2}} \cdot \sin\left(\omega_s t - \dfrac{2\pi}{3}\right). \end{cases} \tag{5}$$

The high-frequency currents $i_{fs\_a}$, $i_{fs\_b}$, and $i_{fs\_c}$ will flow through the dc link of the MMC. The summation $i_{\rm dc\_fs}$ of $i_{fs\_a}$,

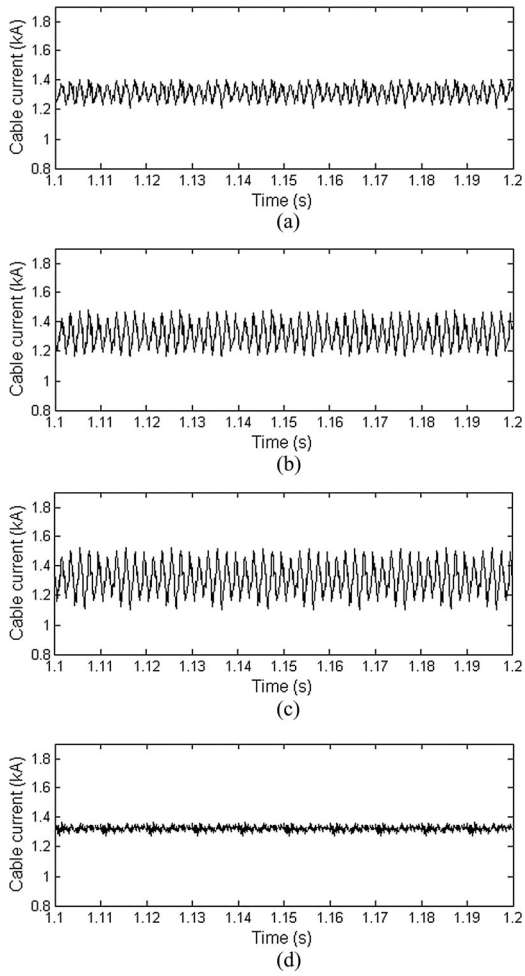


Fig. 11. Cable current $i_{\rm dc}$ of the HVDC system. (a) Without proposed control and $\Delta\theta_a = \Delta\theta_b = \Delta\theta_c = 34°$. (b) Without proposed control and $\Delta\theta_a = \Delta\theta_b = \Delta\theta_c = 32°$. (c) Without proposed control and $\Delta\theta_a = \Delta\theta_b = \Delta\theta_c = 30°$. (d) With proposed control and $k = 2$.

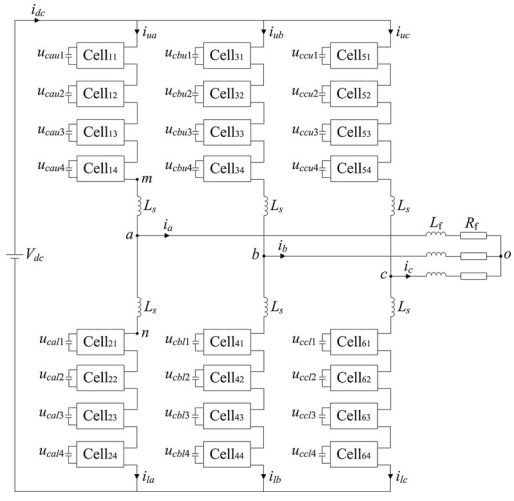


Fig. 12. Block diagram of the experimental circuit.

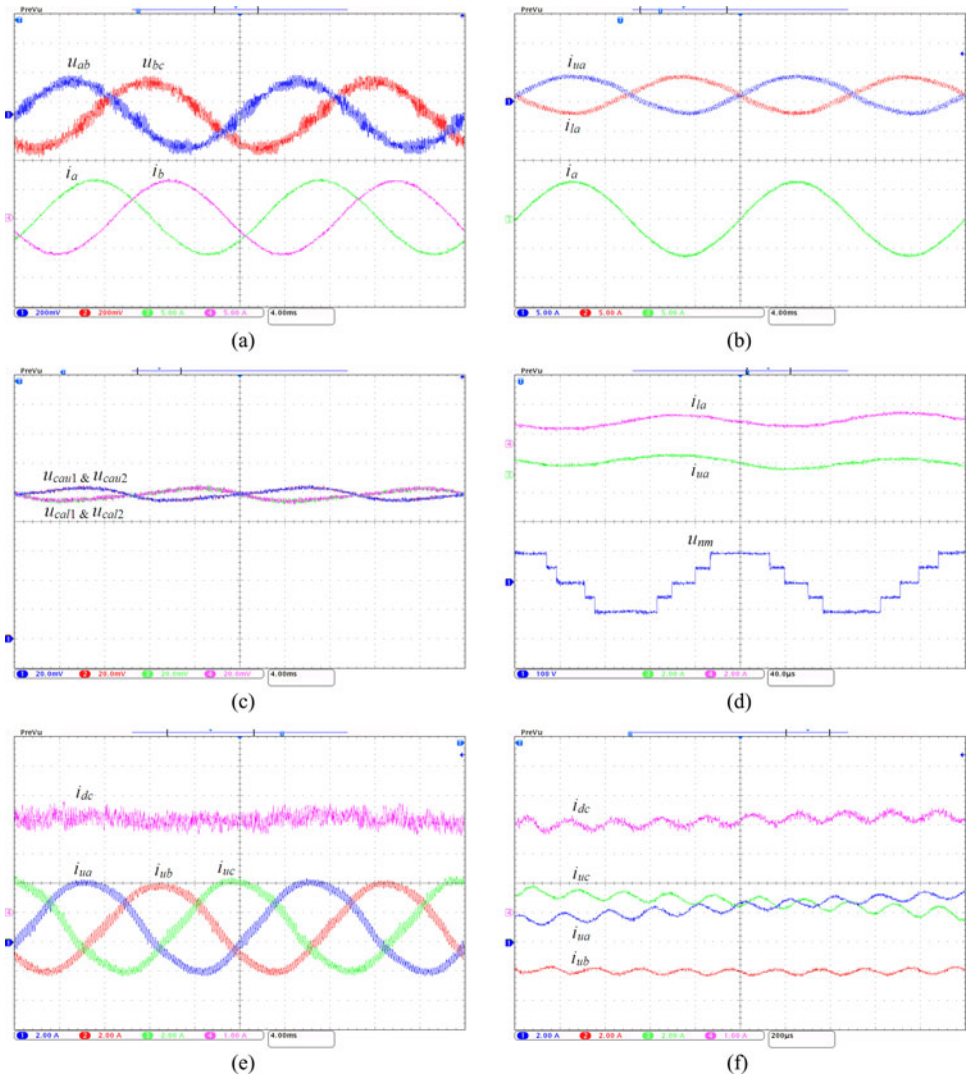


Fig. 13. Measured experimental waveforms under $\Delta\theta_a = \Delta\theta_b = \Delta\theta_c = 60°$. (a) Voltages $u_{ab}$ (100 V/div), $u_{bc}$ (100 V/div) and currents $i_a$ (5 A/div), $i_b$ (5 A/div). Time base is 4 ms. (b) Currents $i_{ua}$ (5 A/div), $i_{la}$ (5 A/div), and $i_a$ (5 A/div). Time base is 4 ms. (c) Voltages $u_{cau_1}$ (10 V/div), $u_{cau_2}$ (10 V/div), $u_{cal_1}$ (10 V/div), and $u_{cal_2}$ (10 V/div). Time base is 4 ms. (d) Currents $i_{ua}$ (2 A/div), $i_{la}$ (2 A/div), and voltage $u_{\rm nm}$ (100 V/div) of phase A. Time base is 40 us. (e) Currents $i_{\rm dc}$ (2 A/div), $i_{ua}$ (2 A/div), $i_{ub}$ (2 A/div), and $i_{uc}$ (2 A/div). Time base is 4 ms. (f) Currents $i_{\rm dc}$ (2 A/div), $i_{ua}$ (2 A/div), $i_{ub}$ (2 A/div), and $i_{uc}$ (2 A/div). Time base is 200 $\mu$s.

$i_{fs\_b}$, and $i_{fs\_c}$ may cause dc-link current ripple, which can be expressed as

$$i_{\mathrm{dc}\_fs}(t) = \frac{2V_c}{\omega_s L_s \pi} \cdot \left[ \cos\left(\frac{\pi}{2}x_a\right) \cdot \frac{\sin\frac{n\Delta\theta_a}{2}}{\sin\frac{\Delta\theta_a}{2}} \cdot \sin(\omega_s t) + \cos\left(\frac{\pi}{2}x_b\right) \cdot \frac{\sin\frac{n\Delta\theta_b}{2}}{\sin\frac{\Delta\theta_b}{2}} \cdot \sin\left(\omega_s t + \frac{2\pi}{3}\right) + \cos\left(\frac{\pi}{2}x_c\right) \cdot \frac{\sin\frac{n\Delta\theta_c}{2}}{\sin\frac{\Delta\theta_c}{2}} \cdot \sin\left(\omega_s t - \frac{2\pi}{3}\right) \right]. \quad (6)$$

From (6), it can be observed that the high-frequency current $i_{\mathrm{dc}\_fs}$ on the dc link of the three-phase MMC can be eliminated with the condition of

$$\cos\left(\frac{\pi}{2}x_a\right) \cdot \frac{\sin\frac{n\Delta\theta_a}{2}}{\sin\frac{\Delta\theta_a}{2}} = \cos\left(\frac{\pi}{2}x_b\right) \cdot \frac{\sin\frac{n\Delta\theta_b}{2}}{\sin\frac{\Delta\theta_b}{2}} = \cos\left(\frac{\pi}{2}x_c\right) \cdot \frac{\sin\frac{n\Delta\theta_c}{2}}{\sin\frac{\Delta\theta_c}{2}} = k \quad (7)$$

where $k$ can be defined as a coefficient. According to (3), $0 \le \cos(x_j\pi/2) \le 1$ ($j = a, b, c$). With the different reference values $x_a$, $x_b$, and $x_c$, the high-frequency current $i_{\mathrm{dc}\_fs}$ on the dc link of the MMC can be eliminated by regulating the phase-shift angles $\Delta\theta_a$, $\Delta\theta_b$, and $\Delta\theta_c$ to satisfy (7).

According to the above analysis, a current ripple elimination control method is proposed, as shown in Fig. 4. The proposed control method is implemented in each period of $2\pi$, as shown

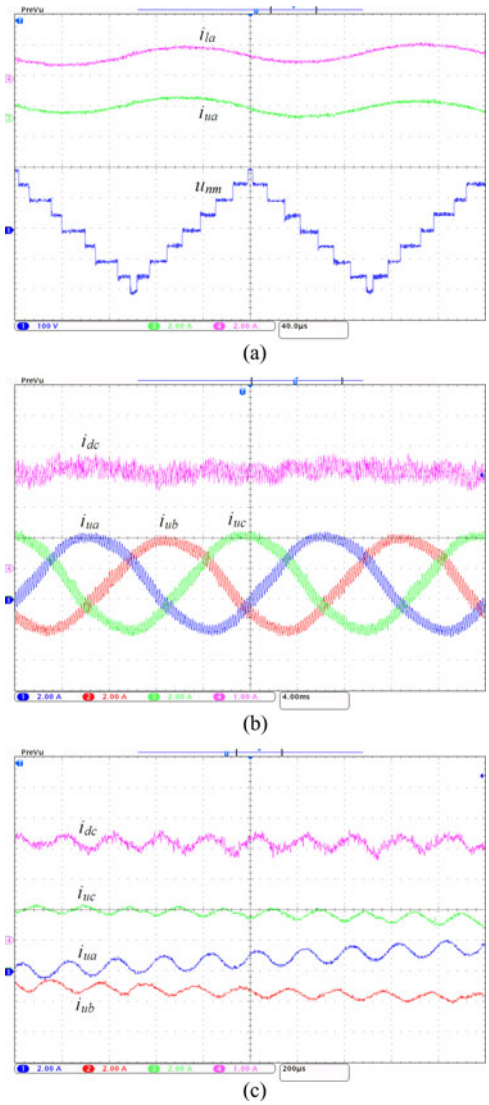


Fig. 14. Measured experimental waveforms under $\Delta\theta_a = \Delta\theta_b = \Delta\theta_c = 50°$. (a) Currents $i_{ua}$ (2 A/div), $i_{la}$ (2 A/div), and voltage $u_{\rm nm}$ (100 V/div) of phase A. Time base is 40 us. (b) Currents $i_{\rm dc}$ (2 A/div), $i_{ua}$ (2 A/div), $i_{\rm ub}$ (2 A/div), and $i_{uc}$ (2 A/div). Time base is 4 ms. (c) Currents $i_{\rm dc}$ (2 A/div), $i_{ua}$ (2 A/div), $i_{ub}$ (2 A/div), and $i_{uc}$ (2 A/div). Time base is 200 $\mu$s.

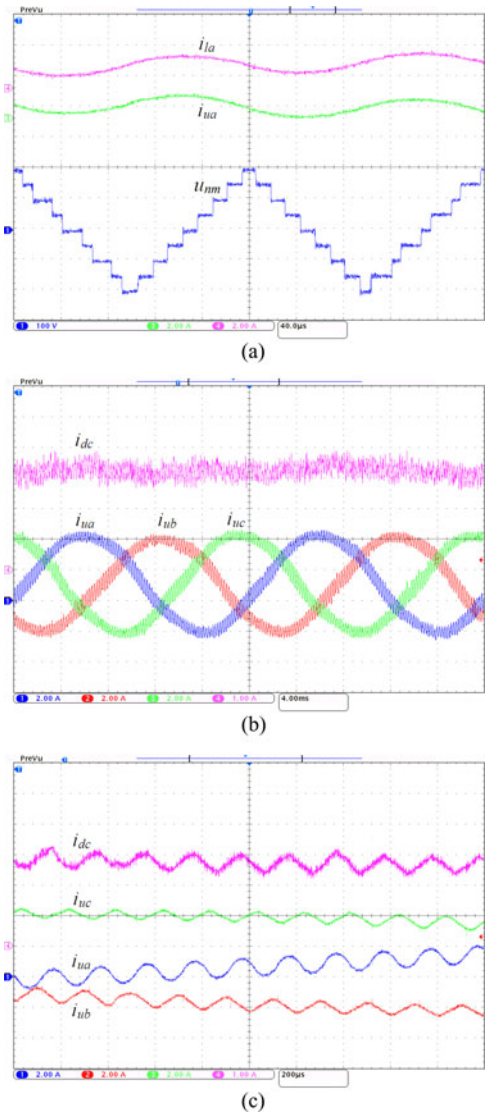


Fig. 15. Measured experimental waveforms under $\Delta\theta_a = \Delta\theta_b = \Delta\theta_c = 45°$. (a) Currents $i_{ua}$ (2 A/div), $i_{la}$ (2 A/div), and voltage $u_{\rm nm}$ (100 V/div) of phase A. Time base is 40 $\mu$s. (b) Currents $i_{\rm dc}$ (2 A/div), $i_{ua}$ (2 A/div), $i_{ub}$ (2 A/div), and $i_{uc}$ (2 A/div). Time base is 4 ms. (c) Currents $i_{\rm dc}$ (2 A/div), $i_{\rm ua}$ (2 A/div), $i_{ub}$ (2 A/div), and $i_{uc}$ (2 A/div). Time base is 200 $\mu$s.

in Fig. 3. Owing to

$$0 \le \frac{\sin\frac{n\Delta\theta_j}{2}}{\sin\frac{\Delta\theta_j}{2}} \le n, (j = a, b, c) \tag{8}$$

there is a maximum value for *k*, which can be expressed as

$$k_{\max} = n \cdot \min\left[\cos(x_a \cdot \pi/2), \cos(x_b \cdot \pi/2), \cos(x_c \cdot \pi/2)\right]. \tag{9}$$

In Fig. 4, a limiter is used to limit the value of $k$ with the maximum value of $k_{\max}$. And then, the phase-shifted angles $\Delta\theta_a$, $\Delta\theta_b$, and $\Delta\theta_c$ can be calculated with (7) corresponding to the different reference values $x_a$, $x_b$, and $x_c$, where a lookup table is used to solve for $\Delta\theta$ in the equation $y = \sin\frac{n\Delta\theta}{2}/\sin\frac{\Delta\theta}{2}$. $y$ and $\Delta\theta$ are the input and output values of the lookup table, respectively. $\Delta\theta_a$, $\Delta\theta_b$, and $\Delta\theta_c$ will be used for the carrier waves of phases A, B, and C in each period of $2\pi$, respectively, so as to eliminate the high-frequency current ripple $i_{\rm dc\_fs}$ on the dc link of the three-phase MMC.

## IV. Simulation Studies

A three-phase MMC system is modeled with the professional tool PSCAD/EMTDC, as shown in Fig. 1, whichis used to verify the proposed current ripple elimination control strategy. The system parameters are shown in the Appendix.

### *B. MMCs Without Proposed Control*

The performance of the three-phase MMC without proposed control is shown in Fig. 5. Fig. 5(a), (c), and (e) shows the carrier waves $W_{ar_1} \sim W_{ar_10}$, $W_{br_1} \sim W_{br_10}$, and + for phases A, B,

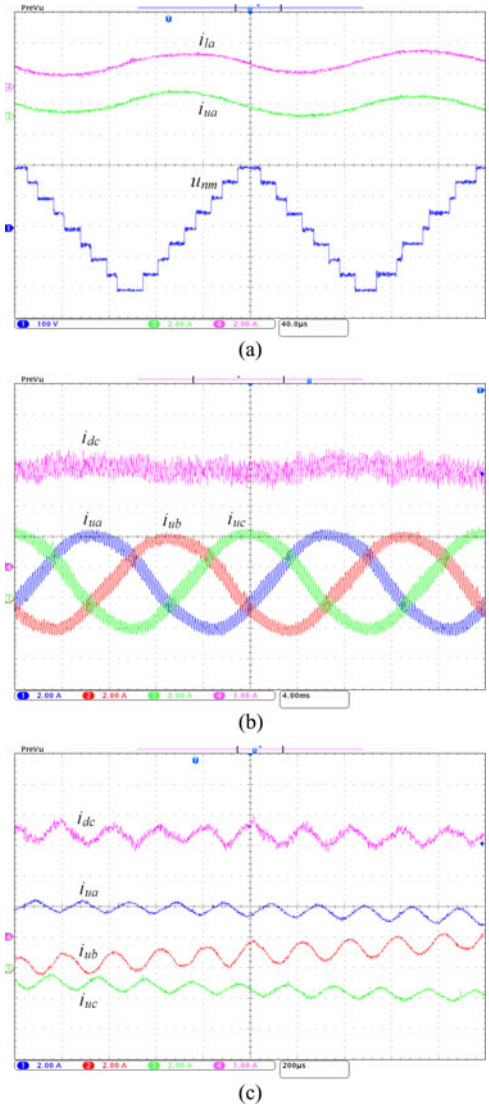


Fig. 16. Measured experimental waveforms under $\Delta\theta_a = \Delta\theta_b = \Delta\theta_c = 40°$. (a) Currents $i_{ua}$ (2 A/div), $i_{la}$ (2 A/div), and voltage $u_{\rm nm}$ (100 V/div) of phase A. Time base is 40 $\mu$s. (b) Currents $i_{\rm dc}$ (2 A/div), $i_{\rm ua}$ (2 A/div), $i_{ub}$ (2 A/div), and $i_{uc}$ (2 A/div). Time base is 4 ms. (c) Currents $i_{\rm dc}$ (2 A/div), $i_{ua}$ (2 A/div), $i_{ub}$ (2 A/div), and $i_{uc}$ (2 A/div). Time base is 200 $\mu$s.

and C, whose middle-points are phase-shifted by an angle of $2\pi/3$, as shown in Fig. 3. Fig. 5(b), (d), and (f) shows the carrier waves for phases A, B, and C in a small time scale, which contains five periods shown in Fig. 3. In addition, each carrier wave for phases A, B and C is phase-shifted by the same angle of 22°. The active and reactive power of the MMC system is 500 and 0 kW, respectively. The circulating current suppression method presented in [16] is used in the MMC. The capacitor voltages of phase A are shown in Fig. 5(g), which are kept balanced. The upper and lower arm currents $i_{ua}$ and $i_{la}$ of phase A are shown in Fig. 5(h). The three-phase upper arm currents $i_{ua}$, $i_{ub}$, and $i_{uc}$ are shown in Fig. 5(i). Owing to the PSC-PWM method, the 1.15-kHz high-frequency component in the arm current with the same frequency to that of the carrier wave is generated, as shown in Fig. 5(k). The ratio of the 1.15-kHz high-frequency component to the 50-Hz fundamental component in the arm current is 10.1%. On the dc link of the MMC, a 1.15-kHz high-frequency current ripple is caused, as shown in Fig. 5(j). From Fig. 5(l), it can be seen that the peak-to-peak value of the current ripple is approximately 0.18 per unit.

Figs. 6(a) and 7(a) show the upper arm currents of the MMC without proposed control under $\Delta\theta$ of 26° and 30°, where the ratio of the 1.15-kHz high-frequency component to the 50-Hz fundamental component in the arm current is 7.3% and 4.7%, respectively. A 1.15-kHz high-frequency current ripple is caused in the dc-link current $i_{\rm dc}$, and the peak-to-peak value of the high-frequency current ripple is 0.14 and 0.09 per unit, respectively.

### B. MMCs With Proposed Control

The performance of the three-phase MMC with the proposed control is shown in Fig. 8, where the coefficient $k$ is 2. Fig. 8(a), (c), and (e) shows the carrier waves $W_{ar_1} \sim W_{ar_10}$, $W_{br_1} \sim W_{br_10}$, and $W_{cr_1} \sim W_{cr_10}$ for phases A, B, and C, whose middle-points are phase-shifted by an angle of $2\pi/3$, as shown in Fig. 3. Fig. 8(b), (d), and (f) shows the carrier waves for phases A, B, and C in a small time scale, which contains five periods shown in Fig. 3. From Fig. 8(a)–(f), it can be seen that the phase-shifted angles of phases A, B, and C vary in different periods. The capacitor voltages of phase A is shown in Fig. 8(g), which is kept balanced. The upper and lower arm currents $i_{ua}$ and $i_{la}$ of phase A are shown in Fig. 8(h). Fig. 8(i) shows the upper arm current $i_{ua}$, $i_{ub}$, and $i_{uc}$. The 1.15-kHz high-frequency component is generated in the arm current, as shown in Fig. 8(k), and the ratio of the 1.15-kHz high-frequency component to the 50-Hz fundamental component in the arm current is 7.7%. Owing to the proposed current ripple elimination control, the 1.15-kHz high-frequency current ripple on the dc link of the MMC is almost eliminated, as shown in Fig. 8(j). The phase-shifted angles $\Delta\theta_a$, $\Delta\theta_b$, and $\Delta\theta_c$ in the proposed current ripple elimination control are shown in Fig. 8(l), which will be sampled in each period and used for control in each period.

Fig. 9 shows the performance of the MMC with the proposed control under $k = 2.5$, where the ratio of the 1.15-kHz high-frequency component to the 50-Hz fundamental component in the arm current is 9.1%. Based on the proposed control, the phase-shifted angles $\Delta\theta_a$, $\Delta\theta_b$, and $\Delta\theta_c$ are shown in Fig. 9(d), which will be sampled and applied in each period to eliminate the 1.15-kHz high-frequency current ripple on the dc link of the MMC, as shown in Fig. 9(b).

### C. Validation With an MMC-Based HVDC System

An MMC-based HVDC system is modeled, as shown in Fig. 10, where the frequency-dependent phase model is applied as the simulation model for cables in PSCAD/EMTDC [27]. The HVDC system parameters and the cable data are listed in the Appendix. In Fig. 10, the MMC 1 is used to keep the dc-link voltage $V_{\rm dc}$ constant as 300 kV, and MMC 2 is used to convert ac to dc and send the power $P_g$ to MMC 1. In the simulation, the HVDC system works at the rated power. Fig. 11(a)–(c) shows the cable current $i_{\rm dc}$ without the proposed control, where the

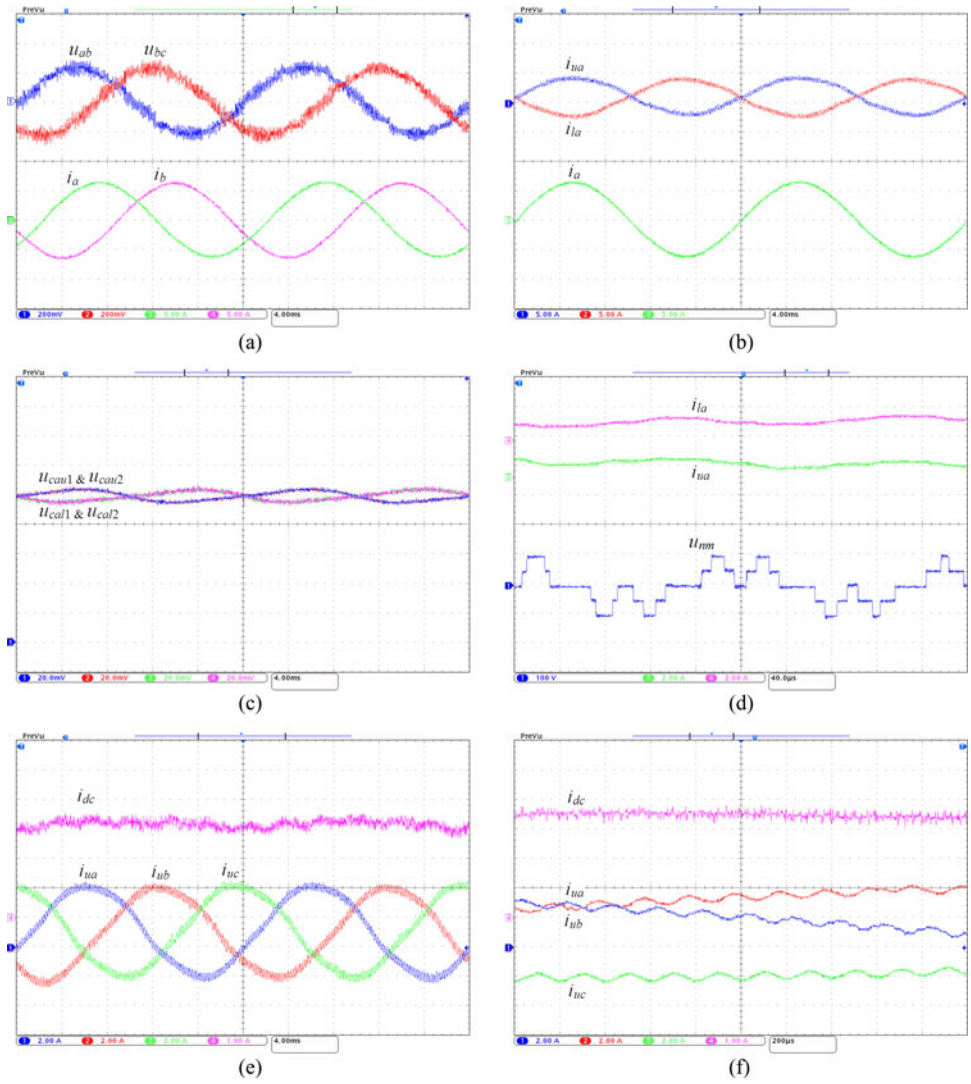


Fig. 17. Measured experimental waveforms under $k = 1$. (a) Voltages $u_{ab}$ (100 V/div), $u_{bc}$ (100 V/div) and currents $i_a$ (5 A/div), $i_b$ (5 A/div). Time base is 4 ms. (b) Currents $i_{ua}$ (5 A/div), $i_{la}$ (5 A/div), and $i_a$ (5 A/div). Time base is 4 ms. (c) Voltages $u_{cau_1}$ (10 V/div), $u_{cau_2}$ (10 V/div), $u_{cal_1}$ (10 V/div), and $u_{cal2}$ (10 V/div). Time base is 4 ms. (d) Currents $i_{ua}$ (2 A/div), $i_{la}$ (2 A/div), and voltage $u_{\rm nm}$ (100 V/div) of phase A. Time base is 40 $\mu$s. (e) Currents $i_{\rm dc}$ (2 A/div), $i_{ua}$ (2 A/div), $i_{ub}$ (2 A/div), and $i_{uc}$ (2 A/div). Time base is 4 ms. (f) Currents $i_{\rm dc}$ (2 A/div), $i_{ua}$ (2 A/div), $i_{ub}$ (2 A/div), and $i_{uc}$ (2 A/div). Time base is 200 $\mu$s.

phase-shifted angles are 34°, 32°, and 30°, respectively. On the dc link of the HVDC system, the 500-Hz high-frequency current ripple is caused. From Fig. 11(a)–(c), it can be seen that the peak-to-peak value of the current ripple is approximately 0.15, 0.23, and 0.31 per unit, respectively. Fig. 11(d) shows the cable current $i_{\rm dc}$ with the proposed control and $k = 2$. Obviously, it can be seen that the 500-Hz high-frequency current ripple on the dc link is eliminated with the proposed control.

## V. Experimental Studies

A three-phase MMC prototype was built in the laboratory, as shown in Fig. 12, where each arm consists of four SMs. The switches and diodes in each cell are the standard IXFK48N60P power MOSFETs. A dc power supply (SM 600–10) is used to support the dc-link voltage. The carrier wave frequency $f_s$ is set as 5 kHz. The experimental circuit parameters are shown in the Appendix.

### A. MMCs Without Proposed Control

The operation of the MMC without proposed control is tested, where the middle-points of the carrier waves $W_{ar_1} \sim W_{ar_4}$, $W_{br_1} \sim W_{br_4}$, and $W_{cr_1} \sim W_{cr_4}$ for phases A, B, and C are phase-shifted by an angle of $2\pi/3$, as shown in Fig. 3. Each carrier wave for phases A, B and C is phase-shifted by the same angle of 60°. Fig. 13(a) shows the voltages $u_{ab}$, $u_{bc}$ and the currents $i_a$, $i_b$. The currents $i_{ua}$, $i_{la}$, and $i_a$ are shown in Fig. 13(b). The capacitor voltages in phases A are shown in Fig. 13(c), which are kept balanced. Owing to the PSC-PWM method, a 5-kHz high-frequency component is generated in the arm current, as shown in Fig. 13(d) and (e). Fig. 13(f) shows three-phase upper arm currents $i_{ua}$, $i_{ub}$, $i_{uc}$, and the

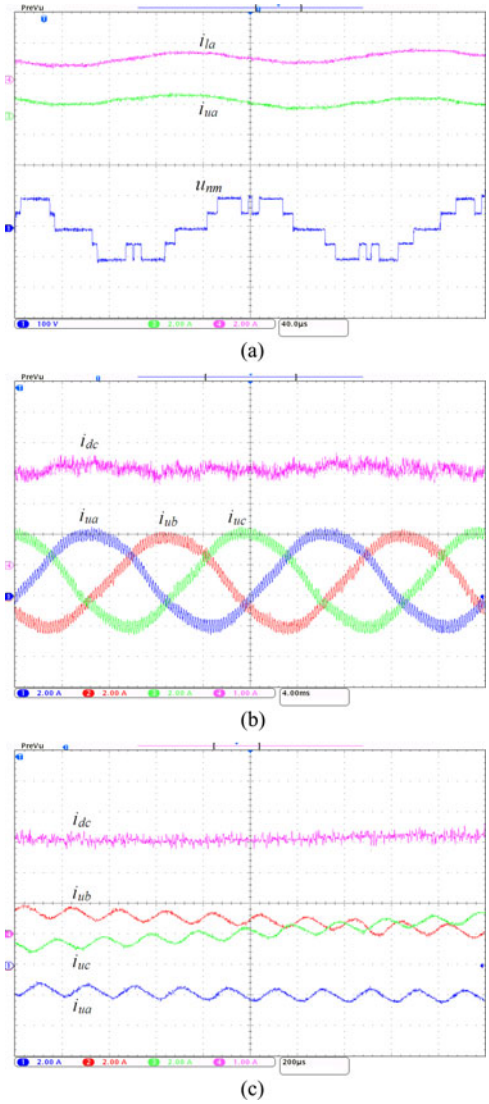


Fig. 18. Measured experimental waveforms under $k = 1.5$. (a) Currents $i_{ua}$ (2 A/div), $i_{la}$ (2 A/div), and voltage $u_{\rm nm}$ (100 V/div) of phase A. Time base is 40 $\mu$s. (b) Currents $i_{\rm dc}$ (2 A/div), $i_{ua}$ (2 A/div), $i_{ub}$ (2 A/div), and $i_{uc}$ (2 A/div). Time base is 4 ms. (c) Currents $i_{\rm dc}$ (2 A/div), $i_{ua}$ (2 A/div), $i_{ub}$ (2 A/div), and $i_{uc}$ (2 A/div). Time base is 200 $\mu$s.

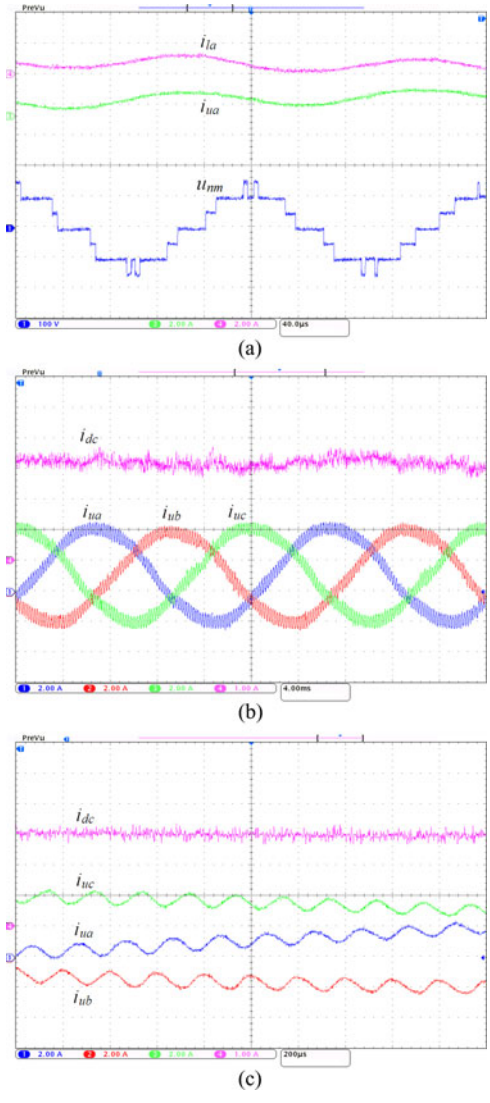


Fig. 19. Measured experimental waveforms under $k = 2$. (a) Currents $i_{ua}$ (2 A/div), $i_{la}$ (2 A/div), and voltage $u_{\rm nm}$ (100 V/div) of phase A. Time base is 40 $\mu$s. (b) Currents $i_{\rm dc}$ (2 A/div), $i_{ua}$ (2 A/div), $i_{ub}$ (2 A/div), and $i_{uc}$ (2 A/div). Time base is 4 ms. (c) Currents $i_{\rm dc}$ (2 A/div), $i_{ua}$ (2 A/div), $i_{ub}$ (2 A/div), and $i_{uc}$ (2 A/div). Time base is 200 $\mu$s.

dc-link current $i_{\rm dc}$ in the small time scale, where the 5-kHz high-frequency component in the arm current is injected into the dc link of the MMC and cause the dc-link current ripple.

Figs. 14–16 show the performance of the MMC under the different phase-shifted angles of 50°, 45°, and 40°, respectively. It can be seen that, along with the reduction of the phase-shifted angle, the fluctuation of the generated high-frequency 5-kHz component in the arm current is increased. A high-frequency 5-kHz current ripple is also caused in the dc-link current $i_{\rm dc}$.

### B. MMCs With Proposed Control

The proposed current ripple elimination control is tested. Fig. 17 shows the performance of the MMC under $k = 1$. The voltage and current of the three-phase MMC are shown in Fig. 17(a) and (b). The capacitor voltages in phase A are shown in Fig. 17(c). The 5-kHz high-frequency component is generated in the arm current of the three-phase MMC, as shown in Fig. 17(d) and (e). Fig. 17(f) shows three-phase upper arm currents $i_{ua}$, $i_{ub}$, $i_{uc}$ and the dc-link current $i_{\rm dc}$ in the small time scale, where the high-frequency 5-kHz ripple in the dc-link current $i_{\rm dc}$ is eliminated with the proposed control strategy.

Figs. 18 and 19 show the MMC performance under $k = 1.5$ and $k = 2$, respectively. Along with the increase of the coefficient $k$, the fluctuation of the 5-kHz high-frequency component in each arm current is increased. The proposed control strategy can effectively eliminate the 5-kHz high-frequency current ripple in the dc-link current $i_{\rm dc}$.

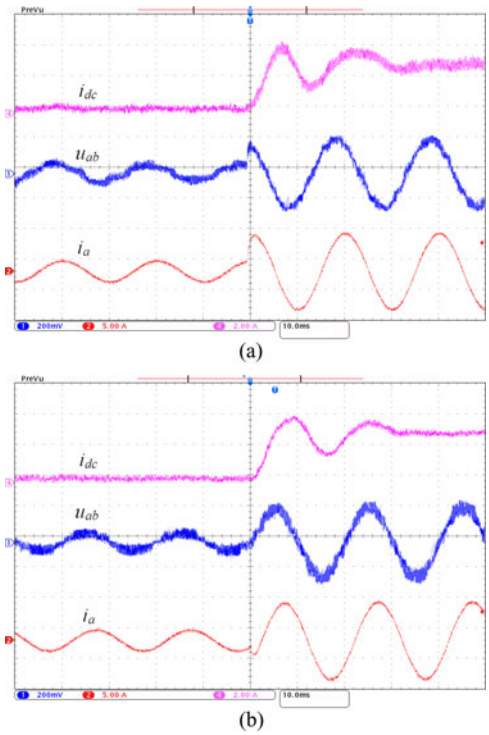


Fig. 20. Measured experimental waveforms including $i_{\rm dc}$ (2 A/div), $u_{ab}$ (100 V/div), and $i_a$ (5 A/div). (a) Without proposed control and $\Delta\theta_a = \Delta\theta_b = \Delta\theta_c = 40°$. (b) With proposed control and $k = 2$. Time base is 10 ms.

### C. Dynamic Performance of MMCs

The dynamic performances of the three-phase MMC under the step change of the modulation index from 0.27 to 0.95 are shown in Fig. 20. Fig. 20(a) shows the results without proposed control and $\Delta\theta_a = \Delta\theta_b = \Delta\theta_c = 40^o$. Fig. 20(b) shows the result with the proposed control under $k = 2$. Owing to the application of the proposed control, the 5-kHz high-frequency ripple in the dc-link current $i_{\rm dc}$ is eliminated. In the steady state of Fig. 20(a) and (b), the ripple of the dc-link current $i_{\rm dc}$ is 30% and 9%, respectively.

## VI. Conclusion

In this paper, a current ripple elimination control strategy is proposed for the three-phase MMC under the PSC PWM scheme. A high-frequency component in the arm current with the same frequency as the carrier wave derived from the PSC PWM scheme is analyzed. The relationship of the generated high-frequency current with the reference signal and the carrier wave's phase-shifted angle is studied. Through the regulation of the phase-shifted angle of the carrier waves in the three phase of the MMC, the caused high-frequency current ripple on the dc-link of the three-phase MMC can be eliminated. A three-phase MMC system is modeled and simulated with PSCAD/EMTDC, and a small-scale three-phase MMC prototype was built in the laboratory. The simulation and experimental results verify the proposed current ripple elimination control.

## Appendix

TABLE III
Parameters of the Three-Phase MMC System

| Parameter | Value |
|---|---|
| Active power *P* (kW) | 500 |
| Grid line-to-line voltage (kV) | 11 |
| Grid frequency (Hz) | 50 |
| Transformer voltage rating | 3 kV/11 kV |
| Transformer leakage reactance | 2.5% |
| DC bus voltage $V_{dc}$ (kV) | 6 |
| Number of SMs per arm *n* | 10 |
| SM capacitance $C_{sm}$ (mF) | 4.7 |
| Arm inductance $L_s$ (mH) | 15 |
| Inductance $L_f$ (mH) | 4 |
| Resistance $R_f$ ($\Omega$) | 0.0157 |
| Carrier frequency $f_s$ (kHz) | 1.15 |

TABLE IV
Parameters of the HVDC System

| Parameter | Value |
|---|---|
| Active power *P* (MW) | 400 |
| Grid line-to-line voltage (kV) | 380 |
| Grid frequency (Hz) | 50 |
| Transformer voltage rating | 150 kV/380 kV |
| Transformer leakage reactance | 20% |
| DC bus voltage $V_{\rm dc}$ (kV) | 300 |
| Number of SMs per arm *n* | 10 |
| SM capacitance $C_{\rm sm}$ (mF) | 1.5 |
| Arm inductance $L_s$ (mH) | 18 |
| Inductance $L_{\rm f}$ (mH) | 6 |
| Resistance $R_f$ ($\Omega$) | 0.0157 |
| Carrier frequency $f_s$ (Hz) | 500 |

TABLE V
Properties of the Cable [27]

| Layer | Material | Thickness (mm) | Resistivity ($\Omega$·m) | Rel. Per-mittivity | Rel. per-meability |
|---|---|---|---|---|---|
| Core | copper | 22 | $1.68 \times 10^{-8}$ | - | 1 |
| Insulator | XLPE | 17 | - | 2.3 | 1 |
| Sheath | Lead | 3 | $2.2 \times 10^{-7}$ | - | 1 |
| Insulator | XLPE | 5 | - | 2.3 | 1 |
| Armor | Steel | 5 | $1.8 \times 10^{-7}$ | - | 10 |
| Insulator | PP | 4 | - | 2.1 | 1 |

TABLE VI
Experimental Circuit Parameters

| Parameters | Value |
|---|---|
| DC power supply $V_{\rm dc}$ (V) | 200 |
| Rated frequency (Hz) | 50 |
| Inductance $L_s$ (mH) | 3.6 |
| DC capacitor $C_{\rm sm}$ (mF) | 2.2 |
| Load inductance $L_f$ (mH) | 1.8 |
| Load resistance $R_f$ ($\Omega$) | 10 |

## REFERENCES


[1] H. Akagi, "Classification, terminology, and application of the modular multilevel cascade converter (MMCC)," *IEEE Trans. Power Electron.*, vol. 26, no. 11, pp. 3119–3130, Nov. 2011.

[2] A. Lesnicar and R. Marquardt, "An innovative modular multilevel converter topology suitable for a wide power range," presented at the IEEE Power Tech. Conf., Bologna, Italy, vol. 3, Jun. 2003.

[3] M. A. Perez, J. Rodriguez, E. J. Fuentes, and F. Kammerer, "Predictive control of AC-AC modular multilevel converters," *IEEE Trans. Ind. Electron.*, vol. 59, no. 7, pp. 2832–2839, Jul. 2012.

[4] M. Hagiwara, K. Nishimura, and H. Akagi, "A medium-voltage motor drive with a modular multilevel PWM inverter," *IEEE Trans. Power Electron.*, vol. 25, no. 7, pp. 1786–1799, Jul. 2010.

[5] M. Hiller, D. Krug, R. Sommer, and S. Rohner, "A new highly modular medium voltage converter topology for industrial drive applications," in *Proc. 13th Eur. Conf. Power Electron. Appl.*, Barcelona, Spain, 2009, pp. 1–10.

[6] B. Gemmell, J. Dorn, D. Retzmann, and D. Soerangr, "Prospects of multilevel VSC technologies for power transmission," in *Proc. IEEE/PES Transmiss. Distrib. Conf. Expo.*, Apr. 21–24, 2008, pp. 1–16.

[7] SIEMENS. Introduction to HVDC Plus (2008). [Online]. Available: https://www.energy-portal.siemens.com/static/hq/en/products_solutions/1652_kn03011203.html

[8] J. Rodríguez, S. Bernet, B. Wu, J. O. Pontt, and S. Kouro, "Multilevel voltage-source-converter topologies for industrial medium-voltage drives," *IEEE Trans. Ind. Electron.*, vol. 54, no. 6, pp. 2930–2945, Dec. 2007.

[9] M. Hagiwara and H. Akagi, "Control and experiment of pulsewidth-modulated modular multilevel converters," *IEEE Trans. Power Electron.*, vol. 24, no. 7, pp. 1737–1746, Jul. 2009.

[10] M. Saeedifard and R. Iravani, "Dynamic performance of a modular multilevel back-to-back HVDC system," *IEEE Trans. Power Del.*, vol. 25, no. 4, pp. 2903–2912, Oct. 2010.

[11] F. Deng and Z. Chen, "A control method for voltage balancing in modular multilevel converters," *IEEE Trans. Power Electron.*, vol. 29, no. 1, pp. 66–76, Jan. 2014.

[12] Z. Li, P. Wang, H. Zhu, Z. Chu, and Y. Li, "An improved pulse width modulation method for chopper-cell-based modular multilevel converters," *IEEE Trans. Power Electron.*, vol. 27, no. 8, pp. 3472–3481, Aug. 2012.

[13] Q. Song, W. Liu, X. Li, H. Rao, S. Xu, and L. Li, "A steady-state analysis method for a modular multilevel converter," *IEEE Trans. Power Electron.*, vol. 28, no. 8, pp. 3702–3713, Aug. 2013.

[14] S. Rohner, S. Bernet, M. Hiller, and R. Sommer, "Modulation, losses, and semiconductor requirements of modular multilevel converters," *IEEE Trans. Ind. Electron.*, vol. 57, no. 8, pp. 2633–2642, Aug. 2010.

[15] M. Guan and Z. Xu, "Modeling and control of a modular multilevel converter-based HVDC system under unbalanced grid conditions," *IEEE Trans. Power Electron.*, vol. 27, no. 12, pp. 4858–4867, Dec. 2012.

[16] Q. Tu, Z. Xu, and L. Xu, "Reduced switching-frequency modulation and circulating current suppression for modular multilevel converters," *IEEE Trans. Power Del.*, vol. 26, no. 3, pp. 2009–2017, Jul. 2011.

[17] A. Antonpoulos, L. Angquist, and H. P. Nee, "On dynamics and voltage control of the modular multilevel converter," in *Proc. Eur. Conf. Power Electron. Appl.*, Barcelona, Spain, 2009, pp. 1–10.

[18] G. S. Konstantinou and V. G. Agelidis, "Performance evaluation of half-bridge cascaded multilevel converters operated with multicarrier sinusoidal PWM techniques," in *Proc. IEEE Conf. Ind. Electron. Appl.*, Xi'an, China, 2009, pp. 3399–3404.

[19] C. Gao, X. Jiang, Y. Li, Z. Chen, and J. Liu, "A dc-link voltage self-balance method for a diode-clamped modular multilevel converter with minimum number of voltage sensors," *IEEE Trans. Power Electron.*, vol. 28, no. 5, pp. 2125–2139, May 2013.

[20] K. Wang, Y. Li, Z. Zheng, and L. Xu, "Voltage balancing and fluctuation-suppression methods of floating capacitors in a new modular multilevel converter," *IEEE Trans. Ind. Electron.*, vol. 60, no. 5, pp. 1943–1954, May 2013.

[21] S. Shao, P. W. Wheeler, J. C. Clare, and A. J. Watson, "Fault detection for modular multilevel converters based on sliding mode observer," *IEEE Trans. Power Electron.*, vol. 28, no. 1, pp. 4867–4872, Nov. 2013.

[22] K. Ilves, S. Norrga, L. Harnefors, and H.-P. Nee, "On energy storage requirements in modular multilevel converters," *IEEE Trans. Power Electron.*, vol. 29, no. 1, pp. 77–88, Jan. 2014.

[23] D. Peftitsis, G. Tolstoy, A. Antonopoulos, J. Rabkowski, J. Lim, M. Bakowski, L. Ängquist, and H. Nee, "High-power modular multilevel converters with SiC JFETs," *IEEE Trans. Power Electron.*, vol. 27, no. 1, pp. 28–36, Jan. 2012.

[24] K. Ilves, A. Antonopoulos, S. Norrga, and H.-P. Nee, "Steady-state analysis of interaction between harmonic components of arm and line quantities of modular multilevel converters," *IEEE Trans. Power Electron.*, vol. 27, no. 1, pp. 57–68, Jan. 2012.

[25] X. Li, Q. Song, W. Liu, H. Rao, S. Xu, and L. Li, "Protection of nonpermanent faults on DC overhead lines in MMC-based HVDC systems," *IEEE Trans. Power Del.*, vol. 28, no. 1, pp. 483–490, Jan. 2013.

[26] D. G. Holmes and T. A. Lipo, *Pulse Width Modulation for Power Converters: Principles and Practice*. Hoboken, NJ: Wiley, 2003.

[27] F. Deng and Z. Chen, "Design of protective inductors for HVDC transmission line within dc grid offshore wind farms," *IEEE Trans. Power Del.*, vol. 28, no. 1, pp. 75–83, Jan. 2013.


**Fujin Deng** (S'10–M'13) received the B.Eng. degree in electrical engineering from the China University of Mining and Technology, Jiangsu, China, in 2005, the M.Sc. degree in electrical engineering from Shanghai Jiao Tong University, Shanghai, China, in 2008, and the Ph.D. degree in energy technology from the Department of Energy Technology, Aalborg University, Aalborg, Denmark, in 2012.

He is currently a Postdoctoral Researcher in the Department of Energy Technology, Aalborg University. His main research interests include wind power generation, multilevel converters, DC grid, high-voltage direct-current technology, and offshore wind farm-power systems dynamics.

**Zhe Chen** (M'95–SM'98) received the B.Eng. and M.Sc. degrees from the Northeast China Institute of Electric Power Engineering, Jilin City, China, and the Ph.D. degree from the University of Durham, Durham, U.K.

He is currently a Full Professor with the Department of Energy Technology, Aalborg University, Denmark, where he is the leader of Wind Power System Research Program. He is the Danish Principle Investigator of Wind Energy of Sino-Danish Centre for Education and Research. His current research interests include power systems, power electronics, electric machines, wind energy, and modern power systems. He has authored or coauthored more than 320 publications in his technical field.

Dr. Chen is an Associate Editor (Renewable Energy) of the IEEE TRANSACTIONS ON POWER ELECTRONICS, a Fellow of the Institution of Engineering and Technology (London, U.K.), and a Chartered Engineer in U.K.